# Structure and Properties of Iron Oxide Nanoparticles Encapsulated by Phospholipids with Poly(ethylene glycol) Tails

**Eleonora V. Shtykova,[†] Xinlei Huang,[‡] Nicholas Remmes,[§] David Baxter,[§] Barry Stein,[||] Bogdan Dragnea,[‡] Dmitri I. Svergun,*[,†,⊥] and Lyudmila M. Bronstein*[,‡]**

*Institute of Crystallography, Russian Academy of Sciences, Leninsky pr. 59, 117333 Moscow, Russia, Department of Chemistry, Indiana University, 800 East Kirkwood Avenue, Bloomington, Indiana 47405, Department of Physics, Indiana University, 727 East Third Street, Bloomington, Indiana 47405, Department of Biology, Indiana University, 1001 East Third Street, Bloomington, Indiana 47405, and European Molecular Biology Laboratory (EMBL), Hamburg Outstation, Notkestrasse 85, D-22603 Hamburg, Germany*

*Received: July 5, 2007; In Final Form: September 17, 2007*

Iron oxide nanoparticles with diameters of 20.1 and 8.5 nm coated with phospholipids containing poly(ethylene glycol) (PEG) tails were studied using small-angle X-ray scattering (SAXS), transmission electron microscopy, dynamic light scattering, and magnetometry. Novel SAXS data analysis methods are applied to build three-dimensional structural models of the nanoparticles coated with PEGylated phospholipids in aqueous solution. The SAXS data demonstrate that the density inside iron oxide nanoparticles is not uniform and depends on the nanoparticle size, which in turn is dependent on the reaction conditions. This heterogeneity is attributed to the presence of two crystalline phases, spinel and wüstite, in the nanoparticles. Because of magnetic properties, the nanoparticles in solution associate in flexible dynamic clusters consisting on average of four individual cores. The magnetometry further supports the SAXS-based models.

## Introduction

Nowadays, interest in magnetic nanoparticles (NPs) is thriving because of applications such as magnetic storage media,[1,2] ferrofluids,[3−5] biosensors,[6] contrast enhancement agents for magnetic resonance imaging,[7−10] bioprobes,[11,12] and so forth. Iron oxide NPs are frequently suggested in biorelated applications because they are easily metabolized or degraded in vivo.[13,14] Magnetic properties are known to be size-dependent;[15−17] therefore, the narrow particle size distribution is one of the imperatives of magnetic NP fabrication. Monodisperse iron oxide NPs can be prepared by thermal decomposition of iron compounds including oxygen-containing ligands such as acetylacetonates,[1,18,19] acetates,[19] or oleates[20,21] in high-boiling solvents containing surfactants.

The second essential step for bioprobe synthesis is the formation of a proper biocompatible shell on the NP surface. Poly(ethylene glycol) (PEG) containing shells are proven to be biocompatible, well soluble in water, and suitable for biomedical applications.[10,22,23] The shell on the NP surface can be created using several methods: by adsorption or growth of polymer or block copolymer chains,[22,24] by formation of NPs in the presence of polymeric surfactants,[25] by attachment of functional ligands,[23,26−28] or by formation of hydrophobic bilayers of amphiphilic molecules with the hydrophobic NP coating (encapsulation into amphiphilic micelles).[29−31]

In this article, we report structure and properties of iron oxide NPs synthesized by decomposition of iron oleates and coated with PEGylated phospholipids via encapsulation. The detailed structure of these particles in aqueous solutions was determined using small-angle X-ray scattering (SAXS). The unique characteristics of SAXS[32] prompted us to apply this method to study structural characteristics of different kinds of novel advanced nanomaterials at resolutions from about 1−100 nm.[33−36] SAXS provides size distributions of metal NPs, their locations in metal-containing polymer matrixes,[37−39] and structural information about internal organization of the entire system.[40−42] In particular, ab initio methods for low-resolution model using SAXS data (e.g., program DAMMIN)[43] were successfully employed for metal-containing polymers.[41,44,45] In the present article, this and other novel methods for SAXS data analysis originally developed for biological systems are for the first time used to build structural models of iron oxide nanoparticles coated with PEGylated phospholipids. Magnetic properties of the samples were also measured and support the conclusions from the SAXS modeling.

## Experimental Section

**1. Materials.** $FeCl_3 \cdot 6H_2O$ (98%), octadecane (99%), and docosane (99%) were purchased from Sigma-Aldrich and used as received. Hexanes (85%), ethanol (95%), and acetone (99.78%) were purchased from EMD and used as received. Chloroform (Mallinckrodt, 100%), oleic acid (TCI, 95%), and oleic acid sodium salt (ScienceLab.com, 95%) were used without purification. 1,2-Distearoyl-*sn*-glycero-3-phosphoethanolamine-*N*-{methoxy[poly(ethylene glycol)]2000} (ammonium salt) (PEG-PL, 2000 Da PEG, Avanti, 99%) was used as received.

**2. Synthesis.** *2.1. Synthesis of Iron Oxide Nanoparticles.* The spherical iron oxide nanoparticles with mean diameters of 20.1 (**NP1**) and 8.5 nm (**NP2**) were synthesized using thermal decomposition of iron oleate by modification of a procedure

* Corresponding authors. E-mail: lybronst@indiana.edu; svergun@embl-hamburg.de.
[†] Institute of Crystallography.
[‡] Department of Chemistry, Indiana University.
[§] Department of Physics, Indiana University.
[||] Department of Biology, Indiana University.
[⊥] EMBL.

10.1021/jp075235c CCC: $37.00 
Published on Web 11/06/2007

published elsewhere.[21,46] In a typical experiment for **NP1**, 2.78 g (3 mmol) of iron oleate complex (dried at 70 °C in a vacuum oven for 24 h),[46] 0.96 mL of oleic acid (3 mmol), and 10 mL of docosane (hydrocarbon $C_{22}H_{46}$, solid at room temperature) were mixed in a three-neck round-bottom reaction flask. The mixture was first heated to 60 °C to melt the solvent and allow the reactants to dissolve under vigorous stirring. Then the temperature was increased to 370 °C with a heating rate of 3.3 °C/min (using a digital temperature controller) under stirring and refluxing for 3 min. During this operation, the initial reddish-brown color of the reaction solution turned brownish-black. The resultant solution was then cooled to 50 °C, and a mixture of 10 mL of hexane and 40 mL of acetone was added into the reaction flask to precipitate the NPs. The NPs were separated by centrifugation and washed 3 times by a mixture of hexane and acetone. After being washed, the resultant NPs were again centrifuged and dissolved in chloroform for long-term storage. Nanoparticles **NP2** were prepared in octadecane at 318 °C, and refluxing was carried out for 30 min. As a precursor, Fe oleate dried at 30 °C in a vacuum oven for 24 h was used.[46]

*2.2. Encapsulation of Iron Oxide Nanoparticles with PEG-PL.* PEG-PL micelles encapsulating iron oxide nanoparticles were formed by using a procedure described elsewhere[30] for QDs. In our earlier work, this procedure was also successfully used for encapsulation of similar iron oxide nanoparticles with carboxy-terminated PEGylated phospholipids.[47] In a typical experiment, 1.7 mg of **NP1** (coated with oleic acid) was dissolved in 1 mL of chloroform and 1.4 mg of PEG-PL was added to the solution. To ensure complete solubilization, the reaction solution was sonicated for 5 min and then chloroform was removed by evaporation. The residual solid was heated in a hot water bath at 80 °C for 5 min, and 1 mL of deionized water was added immediately. After being vigorously stirred for 5 min, a uniform transparent brownish-black aqueous solution was formed. Ultracentrifugation (90000*g*, 2 h, 3 times) was applied to remove excess of PEG-PL. The samples were labeled **NP1-PEG** and **NP2-PEG**, respectively.

**3. Characterization.** Dynamic light scattering (DLS) measurements were carried out with a Zetasizer NanoS, Malvern Instruments. Typically, the diluted sample in water (concentration was in the range 0.05−0.15 mg/mL) underwent sonication for about 10−20 min and filtration with a 0.2-$\mu$m syringe filter before the measurement. Measurement duration was set to be determined automatically, and data were averaged from at least three runs. Intensity and volume distributions of the particle sizes were recorded.

Electron-transparent specimens for transmission electron microscopy (TEM) were prepared by placing a drop of dilute solution onto a carbon-coated Cu grid. Images were acquired at an accelerating voltage of 80 kV on a JEOL JEM1010 transmission electron microscope. Images were analyzed with the Adobe Photoshop software package and the Scion Image Processing Toolkit to estimate NP diameters. Normally, 150−300 NPs were used for analysis. Staining was carried out using uranyl acetate.

X-ray diffraction (XRD) patterns were collected on a Scintag $\theta-\theta$ powder diffractometer with a Cu K$\alpha$ source (0.154 nm).

The synchrotron radiation X-ray scattering data were collected on the X33 camera[48] of the European Molecular Biology Laboratory (EMBL) on the storage ring DORIS III of the Deutsches Elektronen Synchrotron (DESY, Hamburg). Using a MAR image plate detector, we recorded the scattering in the range of the momentum transfer $0.1 < s < 5.0$ nm$^{-1}$, where $s = (4\pi \sin\theta)/\lambda$, $2\theta$ is the scattering angle, and $\lambda = 0.15$ nm is the X-ray wavelength. Two liquid samples **NP1-PEG** and **NP2-PEG** were measured with exposure times of 2 min in a vacuum cuvette to diminish the parasitic scattering. Concentrations of the samples were kept in the range 0.05−0.15 mg/mL (similar to DLS measurements) to minimize interaction of the particles. The scattering profiles were corrected for the background scattering from distilled water and processed using standard procedures.[49] The distance distribution functions $p(R)$ of the iron oxide cores of the nanoparticles were calculated using an indirect transform program GNOM.[50]

The low-resolution shapes and internal structure of the iron oxide cores of the nanoparticles were reconstructed ab initio from the scattering patterns using the program DAMMIN based on the simulated annealing minimization procedure.[43] This program represents the object as an assembly of beads inside a spherical search volume. Starting from a random assembly, DAMMIN employs simulated annealing to build scattering equivalent models fitting the experimental data $I_{exp}(s)$ to minimize discrepancy:

$$\chi^2 = \frac{1}{N-1}\sum_j \left[\frac{I_{exp}(s_j) - cI_{calcd}(s_j)}{\sigma(s_j)}\right]^2 \quad (1)$$

where $N$ is the number of experimental points, $c$ is a scaling factor, and $I_{calcd}(s_j)$ and $\sigma(s_j)$ are the calculated intensity from the model and the experimental error at the momentum transfer $s_j$, respectively.

The structure of the dynamic clusters formed by several iron oxide cores was analyzed by the program SASREF.[51] For this, the scattering amplitudes from DAMMIN models of the individual cores were computed using CRYSOL,[52] and a simulated annealing protocol was employed to find the spatial distribution of several cores minimizing the discrepancy (eq 1) between the experimental scattering data and the curves calculated from the model assemblies. Multiple SASREF runs starting from different initial configurations were performed by varying the number of individual particles in the cluster.

Magnetic measurements were performed on a Quantum Design MPMS XL magnetometer using the systems DC measurement capabilities. Milligram quantities of the sample were placed in a standard gelatin capsule. For zero-field cooling (ZFC) curves, the sample was cooled in a null field (±0.1 Oe) to 4.5 K. A 50 Oe field was then applied, and measurements were taken at regular temperature increments up to 300 K. The sample was then cooled in the 50 Oe field, and the measurements were repeated at the same temperature increments for the field cooling (FC) curves. These ZFC/FC curves were used to establish the blocking temperature and estimate particle volume, which is approximated by:

$$V = \frac{25kT_B}{K} \quad (2)$$

Equation 2 applies to noninteracting uniaxial particles where $k$ is Boltzmann's constant, $K$ is the effective anisotropy constant, and $T_B$ is the blocking temperature.[53] Magnetization measurements were also made at constant temperature well above the blocking temperature by varying fields over a +7 to −7 T range. The shape of these curves was used to estimate the particle size distribution by fitting the curves to a weighted series of Langevin functions.[54] Finally, hysteresis curves were taken well below the blocking temperature when the sample had been cooled in a null field and when the samples had been cooled in a 2 T field.

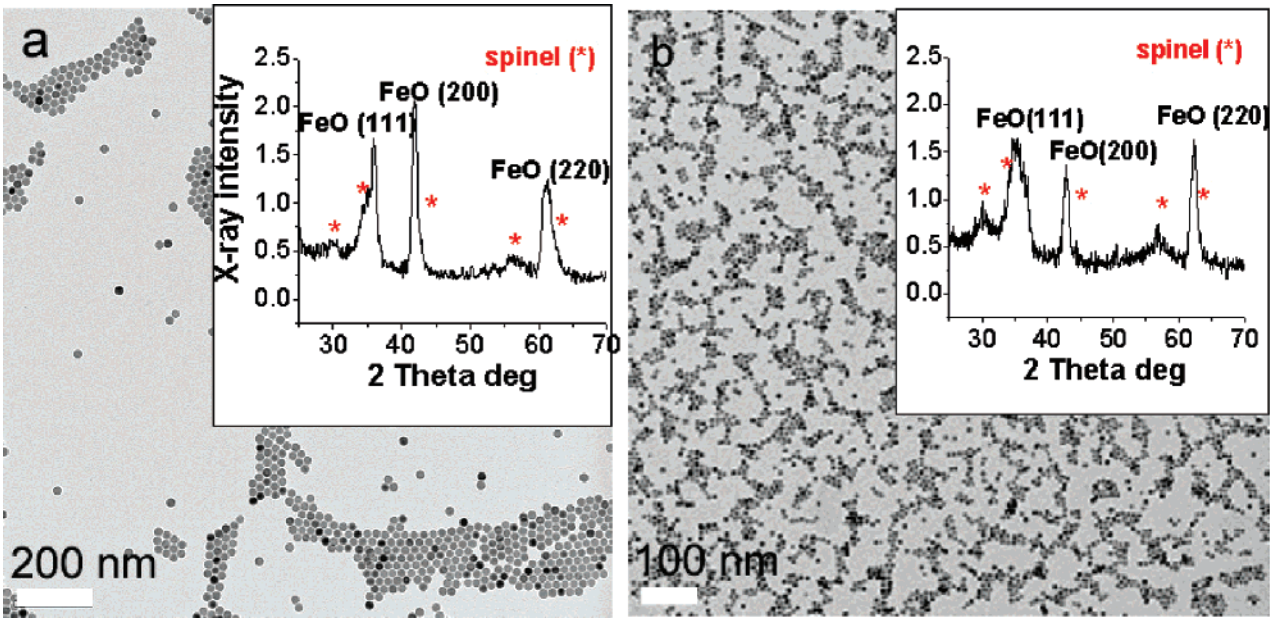


**Figure 1.** TEM images of **NP1** (a) and **NP2** (b) stabilized with oleic acid. Insets show XRD profiles of these NPs.

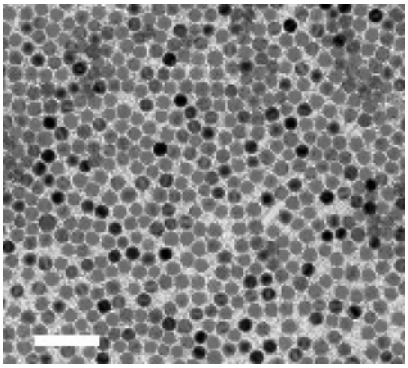

**Figure 2.** TEM image of PEG-PL encapsulated **NP1** (**NP1-PEG**). The sample was negatively stained with uranyl acetate. The scale bar is 100 nm.

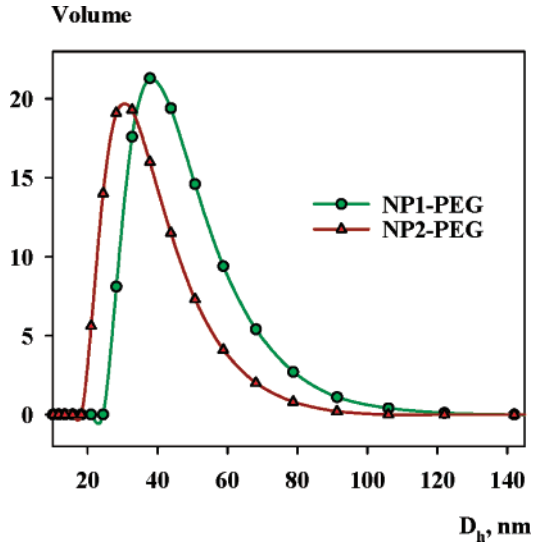


**Figure 3.** DLS volume distributions vs hydrodynamic diameter for **NP1-PEG** and **NP2-PEG**.

## Results and Discussion

**1. Characterization: TEM and DLS.** Monodisperse spherical nanoparticles of 20.1 nm in diameter and standard deviation of 4.1% (**NP1**) and 8.5 nm in diameter and standard deviation of 5.2% (**NP2**) have been prepared using thermal decomposition of iron oleate in the presence of oleic acid as a surfactant in boiling docosane and octadecane, respectively (Figure 1).[46] The XRD data show that iron oxide nanoparticles contain both wüstite ($Fe_{(1-x)}O$) and spinel (most likely $Fe_3O_4$), yet the spinel fraction is higher in **NP2**. In both samples, the wüstite crystals are much larger (the signals are more narrow) than the spinel crystals (the signals are broader) (see also ref 46).

Magnetic nanoparticles coated with oleic acid are hydrophobic. Mixing of the hydrophobic NPs with PEGylated phospholipids (PEG-PL) leads to PEG-PL coated nanoparticles shown in Figure 2. The driving force for encapsulation is hydrophobic interactions between the hydrophobic tails of lipids and oleic acid (the latter are located on the nanoparticle surface). PEG-PL coated NPs are well soluble in water and remarkably stable: no changes were observed for months.

The sample in Figure 2 was negatively stained with uranyl acetate to facilitate visualization of the phospholipid shell that would be difficult to see without staining because of its low electron contrast. However, the stain is evenly spread through the shell toward the NP surface, suggesting that the PEG-PL shell is diffuse and uranyl cations easily penetrate it. The rough estimation of a shortest distance between NPs on the TEM grid surface shows that it is less than 2 nm. Although drying of the shell would cause shrinking, still rough estimation of the shell sizes would suggest larger values. Indeed, the fully extended length of PEG-PL is about 17 nm, while in a crystalline phase, the length of the molecule is 5.2 nm.[55] The length of the fully extended oleic acid tail is about 1.7 nm. Even in the case of full interdigitation of hydrophobic tails of both oleic acid and PEG-PL (then the oleic acid layer does not add to the shell thickness), the sizes of the PEG-PL shell should be expected to be larger than those appearing in Figure 2. This indicates that the shell might be partially squeezed between the particles during the NP self-assembling and drying on the NP surface.

Figure 3 shows the DLS volume distributions vs hydrodynamic diameters ($D_h$) of NPs with the 20.1 and 8.5 nm cores encapsulated in PEG-PL (**NP1-PEG** and **NP2-PEG**, respectively). Because the DLS intensity distributions are strongly dependent on the presence of large particles (the scattering intensity is proportional to the squared volume, i.e., to $R^6$), we

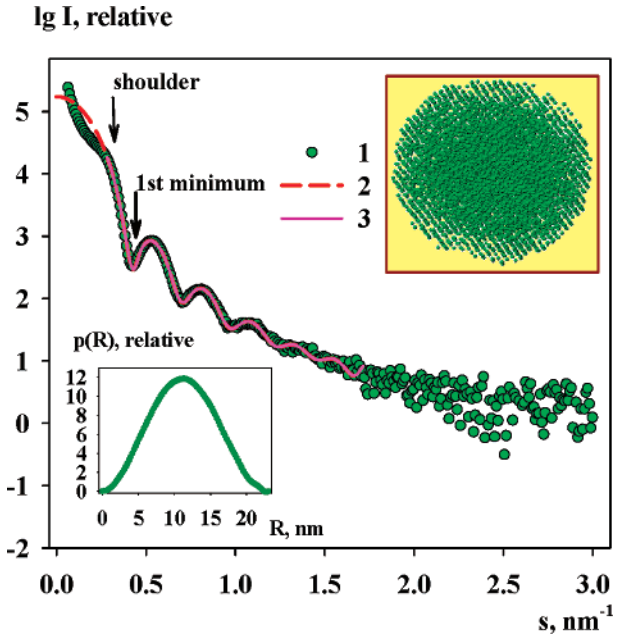


**Figure 4.** Experimental data (1), the curve processed by GNOM and extrapolated to zero scattering angle (2), scattering computed from the bead model (3) for the core of **NP1-PEG**. Insets: bottom left, distance distribution function; top right, ab initio bead model reconstructed from the scattering data.

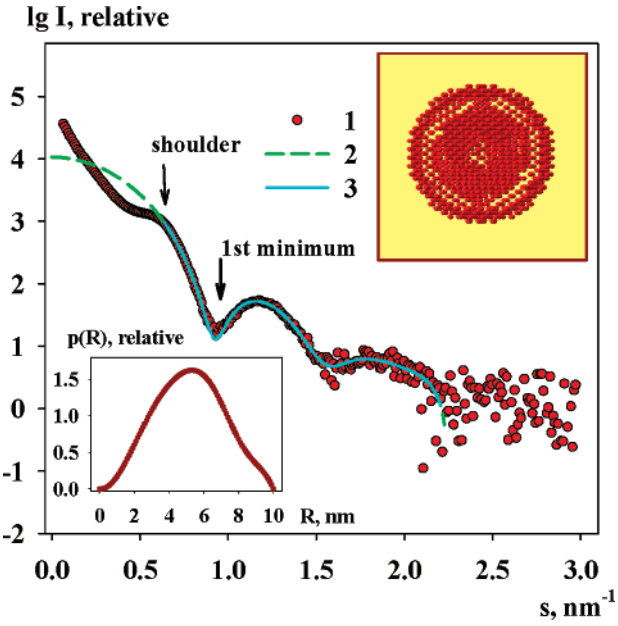


**Figure 5.** Experimental data (1), GNOM curve extrapolated to zero angle (2), scattering patterns computed from the bead model (3) for the core of **NP2-PEG**. Insets: bottom left, distance distribution function; top right, ab initio bead model reconstructed from the scattering data.

used volume distributions of hydrodynamic diameters (the volume is proportional to $R^3$).[56]

Figure 3 displays broad size distributions for both samples with peaks at $D_h = 42$ nm for **NP1-PEG** and 31 nm for **NP2-PEG**. Following the TEM data, both samples should be nearly monodisperse with much smaller nanoparticle sizes. The broad distribution profiles from DLS therefore point to formation of particle clusters due to magnetic interparticle interactions between the nanoparticles. It is thus logical to assume that the effective particle sizes seen by DLS do not correspond to those of individual nanoparticles but rather reflect the influence of the clusters. Further SAXS analysis in Sections 2 and 4 fully confirms this assumption.

**2. Characterization: SAXS.** The structure of NPs in solution was further characterized using SAXS. The experimental scattering profiles from **NP1-PEG** and **NP2-PEG** in Figures 4 and 5 (curve 1) display successive maxima characteristic for monodisperse or slightly polydisperse systems of spherical particles. The average particle radii for the two systems estimated from the position of the first minimum $s_1$ as[32] $R = 4.49/s_1$ are 10.6 ± 0.6 nm for **NP1-PEG** and 4.8 ± 0.3 nm for **NP2-PEG**. These values correlate well with the diameters of the nanoparticles from TEM (20.1 ± 0.8 and 8.5 ± 0.5 nm, respectively).[46] It should be noted that the SAXS-derived values (similar to TEM) refer to the *iron oxide cores only*. These cores have much higher electron density contrast with respect to water than the PEGylated phospholipid shells, so that the latter remain practically invisible for the X-rays.

SAXS profiles in Figures 4 and 5 display shoulders at small angles (around $s = 0.3$ and 0.6 nm$^{-1}$ for **NP1-PEG** and **NP2-PEG**, respectively), which arise from the interference between the neighboring iron oxide particles and unequivocally point to the presence of clusters of such particles in both samples, as was also detected by DLS. The SAXS and the DLS results indicate that the clusters exist in solution, presumably due to the magnetic interactions between the nanoparticles. Since scattering patterns distinctly indicate practically monodisperse

**SCHEME 1: Hypothetical Models of Localization of Iron Oxide Species in NP1-PEG (a) and NP2-PEG (b)**

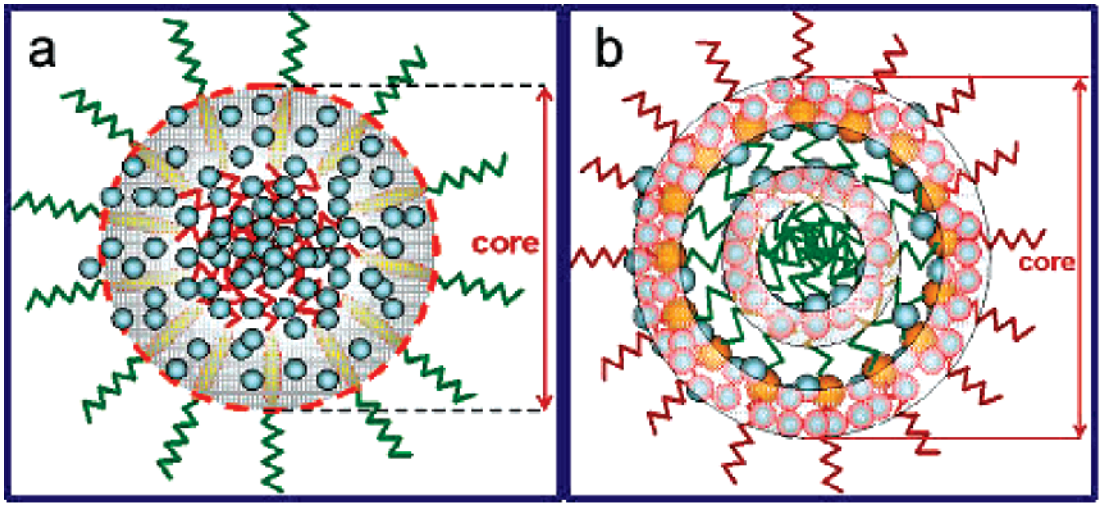

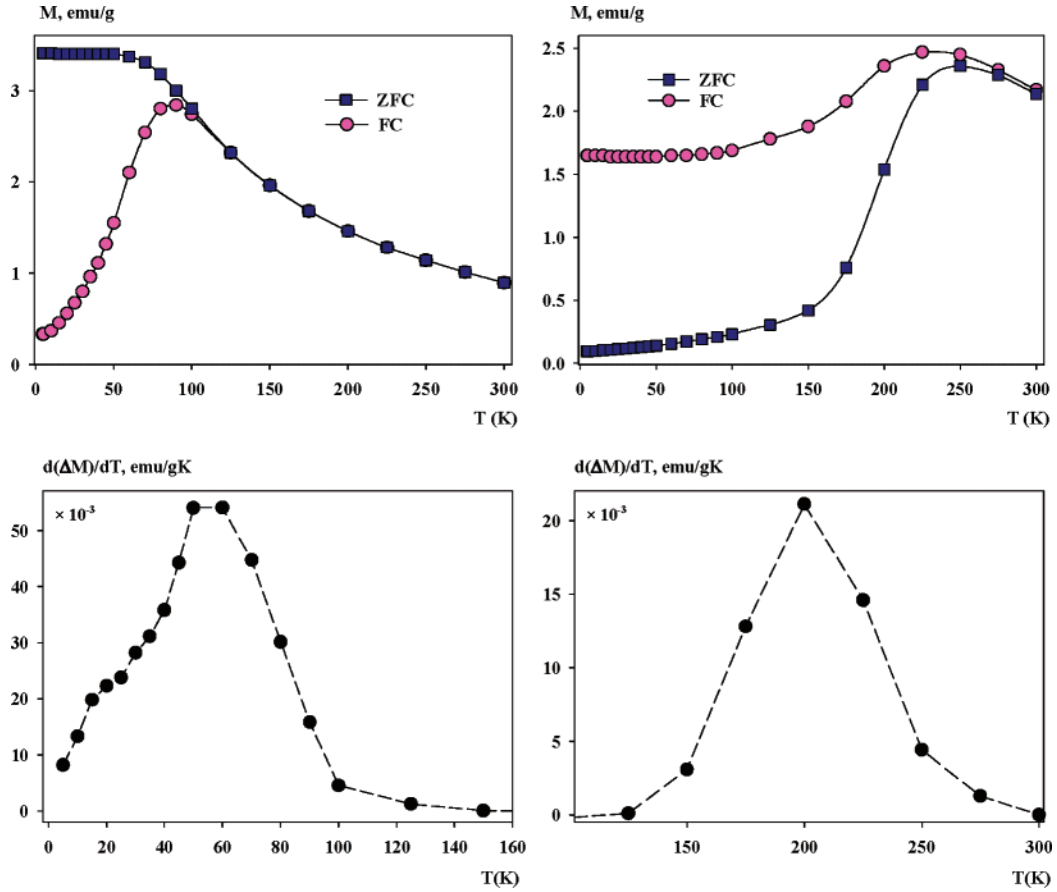


**Figure 6.** ZFC/FC at 50 Oe (top) and derivative of the difference (bottom) for **NP2** (left) and **NP1** (right).

character of the specimens, one can conclude that we do not have micellar aggregates as they are classically viewed, but some kind of temporal associates. The presence of true aggregates in the solutions is very low.

The detailed analysis of the SAXS data consists of two main parts: determination of structural characteristics of the individual nanoparticles using the region of the Bragg peaks on the curves, and investigation of the particle interference reflected by the initial portion of the scattering patterns with the usage of the structural models found at the first stage. Both parts treat different phenomena and, correspondingly, properly fit different parts of the SAXS curves.

The higher-angle portions of the scattering data beyond the interference shoulder reflect the structure of the individual iron oxide core nanoparticles, and the latter can be reconstructed ab initio at low resolution. The appropriate intervals of the experimental curves ($0.30 < s < 1.75$ nm$^{-1}$ for **NP1-PEG**, and $0.6 < s < 2.1$ nm$^{-1}$ for **NP2-PEG**) were processed by the indirect transformation program GNOM[50] to compute the distance distribution functions (insets in Figures 4 and 5). The latter functions were back-transformed to extrapolate the form factor of the individual particle to zero scattering angle (curve 2 in Figures 4 and 5), and the shape was further reconstructed by the program DAMMIN.[43] The typical shapes of the **NP1-PEG** and **NP2-PEG** cores represented by ensembles of densely packed beads (insets in Figures 4 and 5) yield good fits to the experimental data with discrepancy $\chi = 1.5$ and 1.2, respectively (curve 3 in Figures 4 and 5).

Both ab initio models do not have regular spherical shape and display slight anisometry. Before ab initio modeling, we tried to fit the SAXS curves with different simple shape models including disks, and these models failed to fit the experimental data. The major differences between the two types of particles lie in the internal density distribution. These particles are obviously heterogeneous being built from smaller iron oxide nuclei, and the beads in DAMMIN modeling could be considered as these small building blocks. The density of the iron core of **NP1-PEG** (i.e., the density of the beads in the ab initio model in Figures 4 and 5) decreases from the center to the periphery. In contrast, the **NP2-PEG** sample displays a double layer structure with one of the layers on the surface of the particle and a hole in the particle center. These models suggest that the formation of iron oxide particles in the cores of two different systems follows different ways schematically represented in Scheme 1.

We believe that these structural differences can be explained by different reaction temperatures. We assume that the particle growth proceeds by addition of smaller particles (nuclei) to larger growing particles following the aggregative-growth mechanism.[57] The **NP1-PEG** sample is obtained using docosane as a solvent at about 375 °C (bp), while the **NP2-PEG** sample is obtained in octadecane at about 318 °C (bp).[46] We think that at the lower temperature the surfactants may be not fully removed from the nanoparticle interior, leading to lower density in the middle of the nanoparticle and between the first and second layer of comprising small nanoparticles. The other reason for the heterogeneity is the presence of two phases: ferrous oxide wüstite (FeO) and a spinel phase that we assign to magnetite ($Fe_3O_4$),[58] yet wüstite is a dominant phase and its crystallites are larger than those of spinel.[46] These two oxides have different densities thus determining the heterogeneity of the whole particle.

**3. Magnetic Properties.** The ZFC/FC measurements on each sample are shown in Figure 6 with the bottom part showing

the derivative of the ZFC/FC difference with respect to temperature. The region where the ZFC and FC curves overlap the sample is assumed to be superparamagnetic. Within this region, the temperature dependence of the magnetization should follow:

$$M(T) = \frac{NH\mu(T)^2}{3kT} \tag{3}$$

where

$$\mu(T) = \mu_0\lfloor 1 - (T/T_c)^{3/2}\rfloor \tag{4}$$

and where $N$ is the number of particles, $H$ is the applied field, $\mu$ is the moment per particle, and $T_c$ is the ferromagnetic Curie temperature.[59] The inverse of the magnetization can then be estimated as:

$$M^{-1} \cong aT + bT^{5/2} \tag{5}$$

where

$$a = \frac{3k}{HN{\mu_0}^2}; \qquad b = 2aT_c^{-3/2} \tag{6}$$

The average blocking temperature of the **NP1** and **NP2** particles is about 200 and 55 K, respectively (Figure 6). Values obtained for the effective anisotropy of $Fe_3O_4$ magnetic NPs can vary substantially depending on particle size and measurement technique, but generally range from about $2 \times 10^5$ to $4 \times 10^5$ ergs/cm$^3$.[60] This places the average diameter of the magnetic volume of the particles from 22 to 27 nm for the **NP1** sample and from 14 to 18 nm for the **NP2** sample. Strong interparticle interactions, however, are expected to result in a blocking temperature that is slightly higher than that expected from the independent particle model described by eq 2. Additionally, the presence of the wüstite phase could raise the effective anisotropy of the system through exchange bias.[61] Both of these effects would lead to an overestimate of the magnetic volume, which makes the previously quoted values useful only as upper limits. As such, they agree qualitatively with the SAXS and TEM measurements. Additionally, the fact that the ratio of the blocking temperatures for **NP1** and **NP2** is substantially less than the ratio of the volumes predicted by the SAXS and TEM measurements suggests either a more significant interparticle interaction in the **NP2** sample than in the **NP1** sample or a larger effective anisotropy in the **NP2** sample, both of which are likely to be present.

Figure 7 shows inverse magnetization versus temperature for the superparamagnetic regime of data from the **NP2** sample with a least-squares fit using eq 5. The fit gives a value for $T_c$ of $800 \pm 30$ K. Bulk values for $Fe_2O_3$ and $Fe_3O_4$ are 848 and 858 K, respectively.[62] Because of the high blocking temperature of the **NP1** sample, there was insufficient data to perform a similar analysis with this sample.

Figure 8 shows the constant temperature magnetization curve above the **NP2** blocking temperature and the associated fit. The optimal fit was obtained by assuming a normal distribution of large moments and a lognormal distribution of smaller moments. The large moment distribution is assumed to represent the ferromagnetic volume of the particles, and the smaller moments are assumed to represent the paramagnetic response of the wüstite phase, which, though part of the larger particle, rotate independently of the ferromagnetic moment when at this higher temperature. The particle size distribution is obtained by

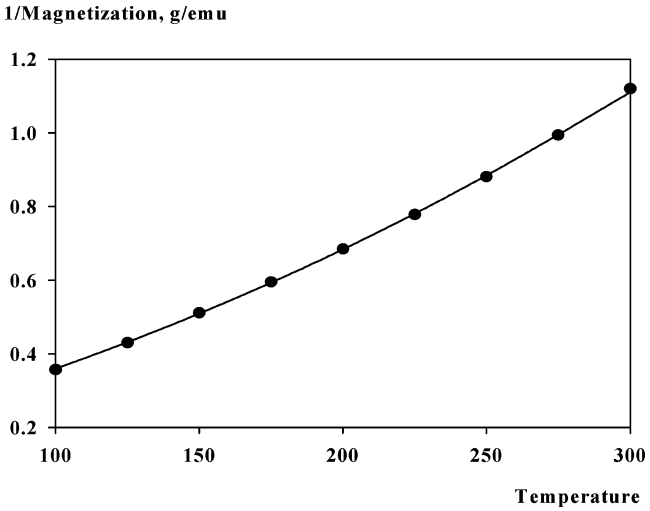


**Figure 7.** Fit of $1/M$ to model for **NP2**.

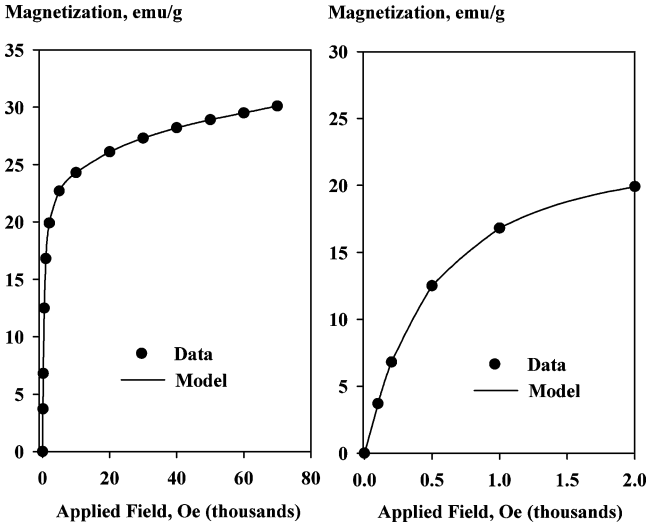


**Figure 8.** **NP2** at 150 K, fit of model to data at high fields (left) and low fields (right).

assuming that the ratio of saturation magnetization to particle size is constant and by using the unweighted average density of FeO and $Fe_3O_4$. This gives an average particle size of about 9.4 nm in diameter with a standard deviation of about 0.5 nm, in very good agreement with the SAXS and TEM measurements. The saturation magnetization of the larger moment distribution of particles is about 20 emu/g with a saturation magnetization for both distributions of about 40 emu/g. While much less than the bulk values of 90 emu/g for $Fe_3O_4$, these saturations are higher than the 7−13 emu/g saturation magnetization of similarly sized $Fe_3O_4$ particles,[60] indicating a substantial presence of the spinel phase.

A similar model did not yield good fits for the **NP1** sample. We speculate that because of the larger sizes of the **NP2** particles and the presence of the wüstite phase, many of the particles in the **NP1** sample may be composed of multiple magnetic domains, preventing any fit that assumes only a narrow moment distribution. The magnetization of the **NP1** samples at 7 T was about 40 emu/g but had not yet saturated. Saturation magnetization due to larger particle moments could be roughly estimated to be at least 30 emu/g, again providing strong support for a substantial spinel presence.

Figure 9 shows the low field portion of ZFC and FC hysteresis curves on the **NP2** sample. The symmetry point of the FC curve shows a distinct offset from zero field of about −350 Oe, which

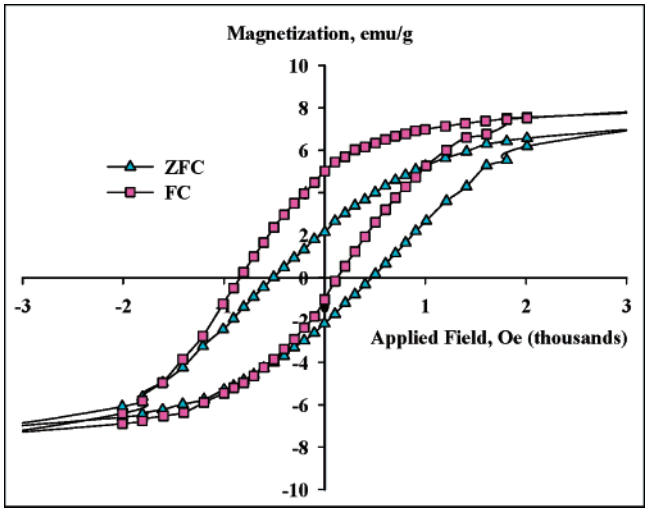


**Figure 9.** ZFC vs FC for **NP2** at 4.5 K.

indicates exchange bias. This exchange bias strongly suggests intimate coupling between the antiferromagnetic wüstite phase and the ferromagnetic spinel phase. This exchange bias is strong evidence that the two phases are present within single particles and provides support for the density variation in the particles as modeled in the SAXS experiments.

**4. Cluster Structure: Comparison of DLS and SAXS Data and Shell Estimation.** The ab initio models of the individual particles were employed to further establish the structure of clusters of the iron oxide particles, the presence of which is clearly revealed by the shoulders in the scattering patterns (Figures 4 and 5). The shape analysis in Section 2 omits the very low angle portions of the data responsible for the interference effects and is of course not able to provide fits to these portions. It was assumed that the clusters may contain several particles, and mutual positions of these particles were established by fitting the entire scattering patterns. The models containing different numbers of individual particles (ranging from two to six particles per cluster) were considered and refined from starting random positions of individual particles using the rigid body modeling program SASREF.[51] For both **NP1-PEG** and **NP2-PEG**, the best results were obtained assuming four particles in the cluster, and the typical models fit the experimental data with discrepancy $\chi = 1.9$ and 1.3, respectively (Figure 10).

The estimate of the average radii of gyration, $R_g$, of the clusters shown in Figure 10 yields 21 nm for **NP1-PEG** and 14 nm for **NP2-PEG**, or, in terms of the diameter, $D$, of approximate spheres 50 and 35 nm, correspondingly, where $D = 2(^5/_3 R_g)^{1/2}$. These values somewhat exceed values of $D_h$ obtained from DLS (42 nm for **NP1-PEG** and 31 nm for **NP2-PEG)** despite the fact that, in SAXS measurements, outer phospholipid shells are not taken into account (Section 2). This could be explained by the flexibility of the clusters diminishing their effective diffusion parameters. Similar effects were observed for flexible objects (polymer chains) in solutions.[63]

For both samples, the observed clusters display an open tetrahedral structure with significant separation between the individual particles. This separation is not surprising given that, as indicated above, SAXS "sees" only the iron oxide cores but not the phospholipid shells, and the obtained models allow one to estimate the shell thickness from the average distance between the neighboring particles in the clusters.

The estimates of the phospholipid shell thickness are $2.4 \pm 0.5$ and $1.4 \pm 0.2$ nm for **NP1-PEG** and **NP2-PEG**, respectively. In both cases, the shell size reveals that hydrophobic chains of oleic acid (surfactant used to stabilize nanoparticles) and PEGylated phospholipids are interdigitated; the size of the hydrophobic bilayer without interdigitation would measure ~3.4 nm. We believe that several factors such as interdigitation (at least partial) of the hydrophobic tails and wrapping of the PEG chains of phospholipids around the core may account for the observed smaller shell thickness compared to that expected from the sizes of phospholipids in solution or even in solid. The ability of PEG chains to wrap around a hydrophobic core was reported in ref 64. We think this ability can be enhanced due to cluster formation and distortion of the shell in the interparticle space.

The observed difference between the thickness of the **NP1-PEG** and **NP2-PEG** shells can be attributed to the different packing of hydrophobic bilayer due to different curvature of the nanoparticle surfaces. The lower curvature of larger particles (**NP1-PEG**) may provide better conditions to fulfill parallel alignment of hydrophobic tails to enhance the hydrophobic interactions and minimize the free energy. This propensity to align leads to the formation of bundles of hydrophobic tails.[65] At lower curvature, this bundling will be rather similar to self-assembled monolayers on flat surfaces where adjacent molecules push for larger stretching of hydrophobic tails and larger angle (90° being the highest) at the flat surface leading to lesser

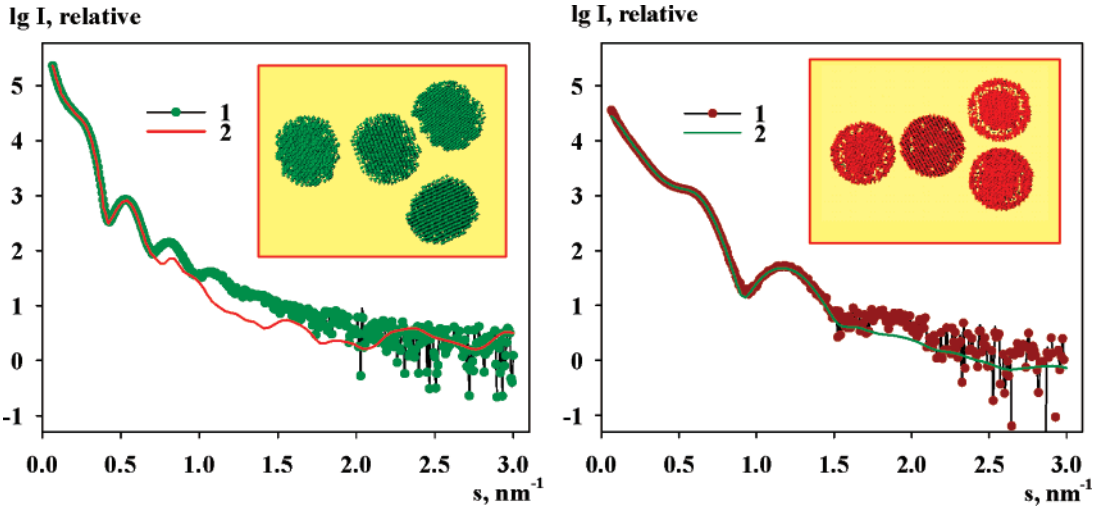


**Figure 10.** Experimental SAXS profile (1) and curve calculated from the model assemblies (2) for the **NP1-PEG** (left) and **NP2-PEG** (right) systems. Insets: complex of corresponding model bodies in different orientations, computed by the program SASREF.

interdigitation and a larger shell size. At higher curvature (smaller particles), the fewer molecules in the bundle may result in a smaller angle of the tails at the surface, full interdigitation, and as a consequence a smaller shell size.

## Conclusions

Water-soluble NPs with core diameters of 20.1 and 8.5 nm were prepared by encapsulation of the NPs with PEGylated phospholipids. The use of advanced modeling methods for the analysis of SAXS patterns allowed us to extract detailed information about the structure of iron oxide particles and their phospholipid shells. It was demonstrated that these particles form well-defined clusters in solution consisting on average from four rather tightly packed individual cores.

The magnetic measurements for the smaller particles reveal exchange bias. This exchange bias suggests intimate coupling between the antiferromagnetic wüstite phase and the ferromagnetic spinel phase. This exchange bias is strong evidence that the two phases are present within a single particle and provides support for the density variation in the particles as modeled in the SAXS experiments.

**Acknowledgment.** This work has been supported, in part, by the NATO Science for Peace Program (Grant SfP-981438), NSF Grant BES-0322767, the IU FRSP Grant, MetaCyt funds, and the European Union FP6 Infrastructures Program (Design Study SAXIER, RIDS 011934).

## References and Notes

(1) Sun, S.; Zeng, H. *J. Am. Chem. Soc.* **2002**, *124*, 8204−8205.
(2) Frolov, G. I. *Tech. Phys.* **2001**, *46*, 1537−1544.
(3) Sestier, C.; Da-Silva, M. F.; Sabolovic, D.; Roger, J.; Pons, J. N. *Electrophoresis* **1998**, *19*, 1220−1226.
(4) Racuciu, M.; Creanga, D. E.; Calugaru, G. *J. Optoelectron. Adv. Mater.* **2005**, *7*, 2859−2864.
(5) Bonini, M.; Wiedenmann, A.; Baglioni, P. *J. Appl. Crystallogr.* **2007**, *40*, s254−s258.
(6) Chang, S. Y.; Zheng, N.-Y.; Chen, C.-S.; Chen, C.-D.; Chen, Y.-Y.; Wang, C. R. C. *J. Am. Soc. Mass Spectrom.* **2007**, *18*, 910−918.
(7) Bulte, J. W.; Kraitchman, D. L. *NMR Biomed.* **2004**, *17*, 484−499.
(8) Mulder, W. J. M.; Strijkers, G. J.; van Tilborg, G. A. F.; Griffioen, A. W.; Nicolay, K. *NMR Biomed.* **2006**, *19*, 142−164.
(9) Medarova, Z.; Pham, W.; Farrar, C.; Petkova, V.; Moore, A. *Nature Med.* **2006**, *13*, 372−377.
(10) Kumagai, M.; Imai, Y.; Nakamura, T.; Yamasaki, Y.; Sekino, M.; Ueno, S.; Hanaoka, K.; Kikuchi, K.; Nagano, T.; Kaneko, E.; Shimokado, K.; Kataoka, K. *Colloids Surf., B* **2007**, *56*, 174−181.
(11) Chemla, Y. R.; Grossman, H. L.; Poon, Y.; McDermott, R.; Stevens, R.; Alper, M. D.; Clarke, J. *Proc. Natl. Acad. Sci. U.S.A.* **2000**, *97*, 14268−14272.
(12) Ivkov, R.; DeNardo, S. J.; Miers, L. A.; Natarajan, A.; Foreman, A. R.; Gruettner, C.; Adamson, G. N.; DeNardo, G. L. Development of tumor targeting magnetic nanoparticles for cancer therapy. In Proceedings of NSTI Nanotech, Boston, MA, May 7−11, 2006; Nano Science and Technology Institute: Cambridge, MA, 2006; pp 21−24.
(13) Hellstern, D.; Schulze, K.; Schopf, B.; Petri-Fink, A.; Steitz, B.; Kamau, S.; Hilbe, M.; Koch-Schneidemann, S.; Vaughan, L.; Hottiger, M.; Hofmann, M.; Hofmann, H.; von Rechenberg, B. *J. Nanosci. Nanotechnol.* **2006**, *6*, 3261−3268.
(14) Briley-Saebo, K.; Bjornerud, A.; Grant, D.; Ahlstrom, H.; Berg, T.; Kindberg, G. M. *Cell Tissue Res.* **2004**, *316*, 315−323.
(15) Talapin, D. V.; Shevchenko, E. V.; Weller, H. In *Nanoparticles;* Schmid, G., Ed.; Wiley-VCH: Weinheim, Germany, 2004; pp 199−230.
(16) Park, T.-J.; Papaefthymiou, G. C.; Viescas, A. J.; Moodenbaugh, A. R.; Wong, S. S. *Nano Lett.* **2007**, *7*, 766−772.
(17) Rong, C.-B.; Li, D.; Nandwana, V.; Poudyal, N.; Ding, Y.; Wang, Z. L.; Zeng, H.; Liu, J. P. *Adv. Mater.* **2006**, *18*, 2984−2988.
(18) Li, Z.; Chen, H.; Bao, H.; Gao, M. *Chem. Mater.* **2004**, *16*, 1391−1393.
(19) Redl, F. X.; Black, C. T.; Papaefthymiou, G. C.; Sandstrom, R. L.; Yin, M.; Zeng, H.; Murray, C. B.; O'Brien, S. P. *J. Am. Chem. Soc.* **2004**, *126*, 14583−14599.
(20) Yu, W. W.; Falkner, J. C.; Yavuz, C. T.; Colvin, V. L. *Chem. Commun.* **2004**, 2306−2307.
(21) Park, J.; An, K.; Hwang, Y.; Park, J.-G.; Noh, H.-J.; Kim, J.-Y.; Park, J.-H.; Hwang, N.-M.; Hyeon, T. *Nat. Mater.* **2004**, *3*, 891−895.
(22) Wan, S.; Huang, J.; Guo, M.; Zhang, H.; Cao, Y.; Yan, H.; Liu, K. *J. Biomed. Mater. Res.* **2007**, *80A*, 946−954.
(23) Gussin, H. A.; Tomlinson, I. D.; Little, D. M.; Warnement, M. R.; Qian, H.; Rosenthal, S. J.; Pepperberg, D. R. *J. Am. Chem. Soc.* **2006**, *128*, 15701−15713.
(24) Kang, Y.; Taton, T. A. *Macromolecules* **2005**, *38*, 6115−6121.
(25) Korth, B. D.; Keng, P.; Shim, I.; Bowles, S. E.; Tang, C.; Kowalewski, T.; Nebesny, K. W.; Pyun, J. *J. Am. Chem. Soc.* **2006**, *128*, 6562−6563.
(26) Zhang, Q.; Gupta, S.; Emrick, T.; Russell, T. P. *J. Am. Chem. Soc.* **2006**, *128*, 3898−3899.
(27) Han, G.; Ghosh, P.; Rotello, V. M. *Nanomedicine* **2007**, *2*, 113−123.
(28) Hostetler, M. J.; Templeton, A. C.; Murray, R. W. *Langmuir* **1999**, *15*, 3782−3789.
(29) Nitin, N.; LaConte, L. E. W.; Zurkiya, O.; Hu, X.; Bao, G. *J. Biol. Inorg. Chem.* **2004**, *9*, 706−712.
(30) Dubertret, B.; Skourides, P.; Norris, D. J.; Noireaux, V.; Brivanlou, A. H.; Libchaber, A. *Science* **2002**, *298*, 1759−1762.
(31) Lim, Y. T.; Lee, K. Y.; Lee, K.; Chung, B. H. *Biochem. Biophys. Res. Commun.* **2006**, *344*, 926−930.
(32) Feigin, L. A.; Svergun, D. I. *Structure Analysis by Small-Angle X-ray and Neutron Scattering;* Plenum Press: New York, 1987.
(33) Dembo, A. T.; Yakunin, A. N.; Zaitsev, V. S.; Mironov, A. V.; Starodubtsev, S. G.; Khokhlov, A. R.; Chu, B. *J. Polym. Sci., Part B: Polym. Phys.* **1996**, *34*, 2893−2898.
(34) Svergun, D. I.; Shtykova, E. V.; Dembo, A. T.; Bronstein, L. M.; Platonova, O. A.; Yakunin, A. N.; Valetsky, P. M.; Khokhlov, A. R. *J. Chem. Phys.* **1998**, *109*, 11109−11116.
(35) Bronstein, L. M.; Platonova, O. A.; Yakunin, A. N.; Yanovskaya, I. M.; Valetsky, P. M.; Dembo, A. T.; Makhaeva, E. E.; Mironov, A. V.; Khokhlov, A. R. *Langmuir* **1998**, *14*, 252−259.
(36) Shtykova, E. V.; Dembo, A. T.; Makhaeva, E. E.; Khokhlov, A. R.; Evmenenko, G. V.; Reynaers, H. *Langmuir* **2000**, *16*, 5284−5288.
(37) Svergun, D. I.; Shtykova, E. V.; Kozin, M. B.; Volkov, V. V.; Dembo, A. T.; Shtykova, E. V. J.; Bronstein, L. M.; Platonova, O. A.; Yakunin, A. N.; Valetsky, P. M.; Khokhlov, A. R. *J. Phys. Chem. B* **2000**, *104*, 5242−5250.
(38) Svergun, D. I.; Kozin, M. B.; Konarev, P. V.; Shtykova, E. V.; Volkov, V. V.; Chernyshov, D. M.; Valetsky, P. M.; Bronstein, L. M. *Chem. Mater.* **2000**, *12*, 3552−3560.
(39) Bronstein, L. M.; Linton, C.; Karlinsey, R.; Ashcraft, E.; Stein, B.; Svergun, D. I.; Kozin, M.; Khotina, I. A.; Spontak, R. J.; Werner-Zwanziger, U.; Zwanziger, J. W. *Langmuir* **2003**, *19*, 7071−7083.
(40) Shtykova, E. V.; Svergun, D. I.; Chernyshov, D. M.; Khotina, I. A.; Valetsky, P. M.; Spontak, R. J.; Bronstein, L. M. *J. Phys. Chem. B* **2004**, *108*, 6175−6185.
(41) Bronstein, L. M.; Sidorov, S. N.; Zhirov, V.; Zhirov, D.; Kabachii, Y. A.; Kochev, S. Y.; Valetsky, P. M.; Stein, B.; Kiseleva, O. I.; Polyakov, S. N.; Shtykova, E. V.; Nikulina, E. V.; Svergun, D. I.; Khokhlov, A. R. *J. Phys. Chem. B* **2005**, *109*, 18786−18798.
(42) Bronstein, L. M.; Dixit, S.; Tomaszewski, J.; Stein, B.; Svergun, D. I.; Konarev, P. V.; Shtykova, E.; Werner-Zwanziger, U.; Dragnea, B. *Chem. Mater.* **2006**, *18*, 2418−2430.
(43) Svergun, D. I. *Biophys. J.* **1999**, *76*, 2879−2886.
(44) Shtykova, E. V.; Shtykova, E. V., Jr.; Volkov, V. V.; Konarev, P. V.; Dembo, A. T.; Makhaeva, E. E.; Ronova, I. A.; Khokhlov, A. R.; Reynaers, H.; Svergun, D. I. *J. Appl. Crystallogr.* **2003**, *36*, 669−673.
(45) Volkov, V. V.; Lapuk, V. A.; Kayushina, R. L.; Shtykova, E. V.; Varlamova, E. Y.; Malfois, M.; Svergun, D. I. *J. Appl. Crystallogr.* **2003**, *36*, 503−508.
(46) Bronstein, L. M.; Huang, X.; Retrum, J. R.; Schmucker, A. L.; Pink, M.; Stein, B. D.; Dragnea, B. *Chem. Mater.* **2007**, *19*, 3624−3632.
(47) Huang, X.; Bronstein, L. M.; Retrum, J. R.; Dufort, C.; Tsvetkova, I.; Aniagyei, S.; Stein, B.; Stucky, G.; McKenna, B.; Remmes, N.; Baxter, B.; Kao, C. C.; Dragnea, B. *Nano Lett.* **2007**, *7*, 2407−2416.
(48) Roessle, M. W.; Klaering, R.; Ristau, U.; Robrahn, B.; Jahn, D.; Gehrmann, T.; Konarev, P.; Round, A.; Fiedler, S.; Hermes, C.; Svergun, D. *J. Appl. Crystallogr.* **2007**, *40*, s190−s194.
(49) Konarev, P. V.; Volkov, V. V.; Sokolova, A. V.; Koch, M. H. J.; Svergun, D. I. *J. Appl. Crystallogr.* **2003**, *36*, 1277−1282.
(50) Svergun, D. I. *J. Appl. Crystallogr.* **1992**, *25*, 495−503.
(51) Petoukhov, M. V.; Svergun, D. I. *Biophys. J.* **2005**, *89*, 1237−1250.
(52) Svergun, D. I.; Barberato, C.; Koch, M. H. J. *J. Appl. Crystallogr.* **1995**, *28*, 768−773.
(53) Cullity, B. D. *Introduction to Magnetic Materials;* Addison-Wesley Series in Metallurgy and Materials; Addison-Wesley: Reading, MA, 1972.

(54) Ferrari, E. F.; da Silva, F. C. S.; Knobel, M. *Phys. Rev. B* **1997**, *56*, 6086−6093.
(55) Avanti Polar Lipids, Inc. http://www.avantilipids.com/.
(56) Malvern Instruments, Ltd. http://www.malvern.com/.
(57) Besson, C.; Finney, E. E.; Finke, R. G. *J. Am. Chem. Soc.* **2005**, *127*, 8179−8184.
(58) Casula, M. F.; Jun, Y.-W.; Zaziski, D. J.; Chan, E. M.; Corrias, A.; Alivisatos, A. P. *J. Am. Chem. Soc.* **2006**, *128*, 1675−1682.
(59) Goya, G. F.; Berquó, T. S.; Fonseca, F. C.; Morales, M. P. *J. Appl. Phys.* **2003**, *94*, 3520−3528.
(60) Lima, E.; Brandl, A. L.; Arelaro, A. D.; Goya, G. F. *J. Appl. Phys.* **2006**, *99*, 083908/1−083908/10.
(61) Nogués, J.; Sort, J.; Langlais, V. V. S.; Suriñach, S.; Muñoz, J. S.; Baró, M. D. *Phys. Rep.* **2005**, *422*, 65−117.
(62) Frederikse, H. P. R. In *CRC Handbook of Chemistry and Physics*, 87th ed., Internet version; Lide, D. R., Ed.; Taylor and Francis: Boca Raton, FL, 2007.
(63) Di Cola, E.; Waigh, T. A.; Trinick, J.; Tskhovrebova, L.; Houmeida, A.; Pyckhout-Hintzen, W.; Dewhurst, C. *Biophys. J.* **2005**, *88*, 4095−4106.
(64) Lo Celso, F.; Triolo, A.; Bronstein, L.; Zwanziger, J.; Strunz, P.; Lin, J. S.; Crapanzano, L.; Triolo, R. *Appl. Phys. A* **2002**, *74*, S540−S542.
(65) Luedtke, W. D.; Landman, U. *J. Phys. Chem. B* **1998**, *102*, 6566−6572.